THE JOURNAL OF PHYSICAL CHEMISTRY C
A JOURNAL OF THE AMERICAN CHEMICAL SOCIETY

pubs.acs.org/JPCC Article

Thermodynamics and Catalytic Activity of Ruthenium Oxides Grown on Ruthenium Metal from a Machine Learning Atomic Simulation

Published as part of The Journal of Physical Chemistry virtual special issue "Energy and Catalysis in China".

Ze-Yi Zhu, Ye-Fei Li,* Cheng Shang, and Zhi-Pan Liu*

Cite This: https://doi.org/10.1021/acs.jpcc.1c04858 Read Online

ABSTRACT: Ru is a poor catalyst for oxidizing CO under ultra-high-vacuum conditions but exhibits high catalytic activity under ambient O_2 pressure. The system is thus regarded as a prototypical system to understand the catalysis of oxides grown on metal. While previous works focus on either bulky metal or bulky oxides, here, we explore the atomic structure of Ru/RuO_2 interfaces and the active site for CO oxidation by using stochastic surface walking global optimization combined with a global neural network potential (SSW-NN) method. Five Ru/RuO_2 interfaces are identified with the modified phenomenological theory of martensitic crystallography, and the two most stable interfaces are Ru(10$\bar{1}$0)//RuO_2(101) and Ru (0001)//RuO_2(101), both involving the less stable oxide (101) plane. By gradually growing RuO_x on Ru(10$\bar{1}$0) and evaluate the thermodynamics, we now complete the atomic picture for oxide growth on Ru metal. The oxide starts to form after 1.75 ML O coverage, and a thin film of RuO_2(101) appears immediately after 2 ML O coverage; these RuO_x thin layers are, however, thermodynamically unstable and tend to aggregate into thick RuO_2 islands due to the >4% lattice mismatch. Importantly, our catalytic activity analyses for CO oxidation on different surface sites demonstrate that the metastable thin layer RuO_2 on Ru is catalytically even more active than bulky oxide surfaces due to the lattice compression of the oxide film. These results indicate the significance to search for metastable structures at phase boundaries in real catalysts. The advent of global neural network simulations provides a viable route to probe the complex catalysis phenomena occurring at phase boundaries/junctions.

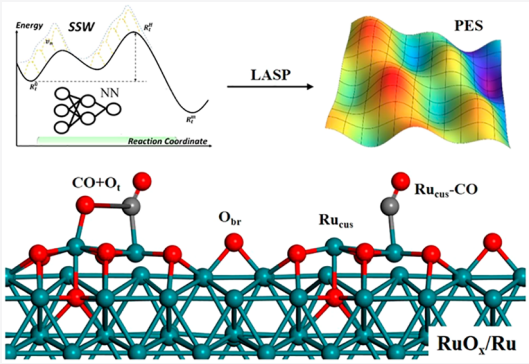

1. INTRODUCTION

Ruthenium (hexagonal close packed metal, hcp) is notably one of the poorest metal catalysts among the late transition metals for oxidizing CO under conditions of low and medium oxygen coverages. However, the CO oxidation activity increases by several orders in excess O_2, which becomes even higher than that in Pt, Pd, and Rh.[1−3] The intriguing findings have raised considerable interests to reveal the structure origin for Ru catalyst in contact with O_2. To date, most experiments have observed the formation of RuO_2 (136 $P4_2/mnm$, rutile),[2] the stoichiometrically most stable form of Ru oxide, on Ru metal, and thus suggest that CO oxidation occurs on RuO_2 crystal surfaces, e.g., RuO_2(110).[1] It however remains unclear how RuO_2 grows on Ru and whether the transition structures, e.g., thin film of surface oxides, might also account for catalytic activity.

In contrast to the versatile oxidation state of the Ru element ($4d^7\ 5s^1$, from −II to +VIII), the surface redox chemistry of Ru metal oxidation appears to be straightforward, i.e., forming RuO_2, but a great structure complexity lies at the interface of surface oxidation. Although theoretical studies predict the corundum structure of Ru_2O_3 (167 R-3C), Ru(III) oxide is never detected in experiments. The high-oxidation-state oxides, RuO_3 and RuO_4, have also been searched, and it is found that RuO_4, a volatile and toxic catalyst often used in organic synthesis, is prone to decompose into RuO_2 and O_2 above 373 K.[2] It is well established in experiments that, by exposing the single crystalline Ru surfaces to molecular oxygen (10^6 L, at 10^{-5} mbar), a well-ordered RuO_2 film is grown at temperatures ranging from 600 to 750 K.[4] However, the orientation of RuO_2 grown on the Ru substrate is not certain, where both the experimental conditions and the orientation of the Ru substrate seem to matter. For instance, Over et al. reported that RuO_2 grows preferentially in the (110) orientation on Ru(0001) under surface science conditions (700 K, 10^{-2} mbar),[1] but it adopts the (100) orientation on Ru(10$\bar{1}$0).[5]

Received: June 2, 2021
Revised: July 2, 2021

Under the electrochemical oxidation conditions, a different orientation of RuO_2, i.e., a rough $RuO_2(100)$ film, was found to grow on Ru(0001).[4] Other orientations, including (101)[6] and (111),[7] were also observed on Ru(0001) and Ru($10\bar{1}0$) surfaces.

Although the interfacial structure of Ru/RuO_2 is unknown, RuO_2 surfaces, particularly $RuO_2(110)$, have been well characterized in experiments. $RuO_2(110)$ has the lowest surface energy, which is followed by the other two less stable surfaces, (101) and (100) (the surface energies are 1.14, 1.22, and 1.39 J/m^2 for (110), (101), and (100), respectively) as determined by density functional theory (DFT) calculations.[2] With the help of low-energy electron diffraction (LEED) and DFT calculations, the surface structure of $RuO_2(110)$ has been determined. It exposes two types of uncoordinated surface atoms: the bridging oxygen atoms (O_{br}) coordinated to two Ru atoms underneath, and the coordinatively unsaturated Ru atoms (Ru_{cus}), which are coordinated to five O atoms.[1] The additional O atoms, e.g., from the dissociative oxygen adsorption, can further attach to the top site of Ru_{cus},[9] forming the terminal O (O_t). The high CO oxidation ability of $RuO_2(110)$ has been attributed to the CO at the Ru_{cus} site reacting with the bridging O or the terminal O depending on the O_2 pressure, where the calculated reaction barriers (~0.8 eV) are significantly lower than that for the CO oxidation on Ru(0001) (>1.3 eV). By comparing $RuO_2(110)$ with (100) and (101) surfaces, the coordinated unsaturated surface atoms (Ru_{cus} and O_{br}) are well separated on $RuO_2(110)$ but share the coordinations on the other two surfaces.[5,8,10] In fact, the (100) and (101) RuO_2 surfaces were found to undergo severe surface reconstruction under O-rich conditions. A superposition of (1 × 1) domains and $c(2 \times 2)$ domains occurs on $RuO_2(100)$,[5] while a (1 × 2) superstructure appears on $RuO_2(101)$.[8] The most stable surface structure for these less stable RuO_2 surfaces is not well characterized at the atomic level.

In this work, we aim to resolve the microstructure of RuO_x phases grown on Ru metal by combining machine-learning-based global optimization[11−14] and the modified phenomenological theory of martensitic crystallography (PTMC) method. Our investigation starts from the determination of the RuO_x bulk phase diagram and continues to the exploration of RuO_x/Ru interface structures and finally to the calculation of CO oxidation activity. Rich insights into RuO_x bulk and interface structures are thus obtained. Our results demonstrate that thin oxide films grown on metal could have the highest catalytic activity compared to both bulky metal surfaces and oxide surfaces.

2. METHODS

2.1. Machine-Learning-Based Global Structure Search. The machine learning atomic simulation developed recently, namely, stochastic surface walking based on global neural network (G-NN) potential (SSW-NN), is utilized to search for all bulk and interface structures. The SSW-NN method is implemented in the large-scale atomic simulation with neural network potential (LASP) code,[12,15,16] which incorporates multiple functionalities from data generation, G-NN potential construction to atomic simulations with G-NN potential. The G-NN potential is trained by self-learning of the global potential energy surface data set generated from the SSW global structure search. The training is iteratively carried out until the G-NN potential is robust enough to describe the global PES quantitatively. The methods have been described in our recent publications, and more details can be found in the Supporting Information (SI).

This work generates the first Ru−C−H−O quaternary G-NN potential, where the global PES data set includes a range of different structures (cluster, layer, and bulk), different compositions, and different supercells up to 145 atoms/cell. The data set is detailed in Table S1. In total, more than 10^7 structures were generated by SSW-NN during G-NN potential generation, and 46 731 of them were calculated by DFT and used as the final global data set for G-NN potential training. The root-mean-square (rms) errors of the G-NN potential are 7.684 meV/atom and 0.200 eV/Å with respect to DFT values. We also benchmarked the G-NN calculations against DFT results for important structures, which shows the energy rms error of 8.343 meV/atom (see Table S2). Such a small error suggests that the G-NN PES provides a good description of DFT PES of RuO_x and is accurate enough for predicting the low-energy structures on PES.

2.2. Method to Identify the Likely Orientation Relations in Heterojunctions. The modified phenomenological theory of martensitic crystallography (PTMC) was utilized to determine the possible heterojunction structures between Ru and RuO_x. The PTMC is one of the oldest phase transformation theories, which is developed to explain the phase transition between face-centered cubic austenite (γ-Fe) and body-centered cubic martensite (α-Fe) discovered by Bain in 1924.[17] PTMC takes the existence of the invariant plane as the basic geometric constraint for searching for a phase transition pathway. In the invariant plane, the lattice is neither stretched nor compressed during the phase transition. The key step of PTMC is thus to determine the orientation of the invariant plane through the lattice correspondence **F** matrix, which is given by eq 1

$$\mathbf{TF} = \mathbf{M} \tag{1}$$

where **T** and **M** are the lattice parameter matrix of two crystals, both being (3 × 3) matrices.

The idea of the invariant plane and corresponding mathematical methods in PTMC can be adapted to predict the OR (orientation relationship) in heterojunctions since a stable interface also requires the good lattice match between phases. In the martensitic transformation of materials, the lattice correspondence is explicitly defined by the phase transition channel with the low energy barrier. However, for heterojunctions, any lattice correspondence between two different materials is in principle allowed since it is irrelevant to the phase transition. Because the definition of a unit cell is not unique in the periodic system, there are an infinite number of lattice correspondences. Therefore, the basic procedure to predict the OR in heterojunctions is to sample as many lattice correspondences as possible by changing the definition of the unit cell and then to calculate the orientation of the invariant plane through PTMC. The calculation details of OR in heterojunctions can be found in the Supporting Information and our previous publications.[18−20]

2.3. DFT Calculations. All DFT calculations were performed using the periodic plane-wave method with the projected augmented wave (PAW)[21] scheme, as implemented in the Vienna ab initio simulation package (VASP).[22] The Perdew−Burke−Ernzerhof (PBE) functional at the generalized gradient approximation (GGA)[23] was employed for all the calculations with a plane-wave basis set of 450 eV cutoff. The Monkhorst−Pack k-mesh was 25 times the reciprocal lattice

https://doi.org/10.1021/acs.jpcc.1c04858
J. Phys. Chem. C XXXX, XXX, XXX−XXX

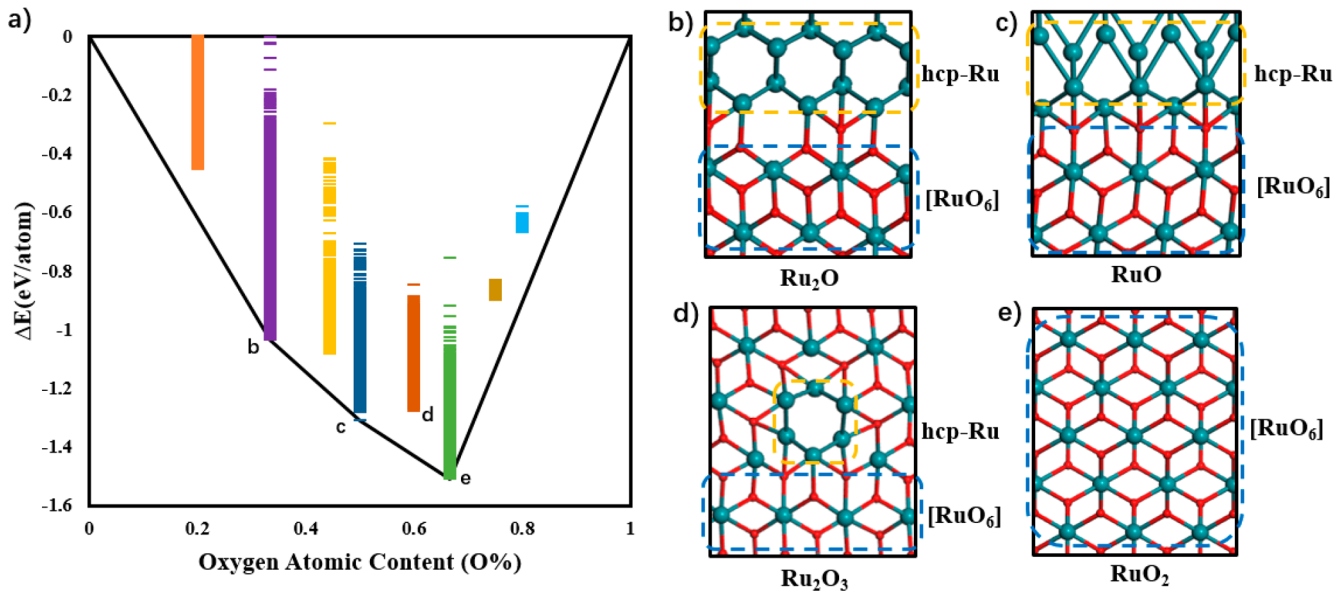

Figure 1. (a) Thermodynamic convex hull diagram for RuO_x with respect to the Ru metal and O_2 molecule. The energy spectrum from SSW-NN structures for each composition is shown as the color bar. (b−e) Four representative structures for the GM of RuO_x obtained from the SSW-NN search of $Ru_{20}O_{10}$(O% = 0.333), $Ru_{20}O_{20}$(0.5), $Ru_{20}O_{30}$(0.6), and $Ru_{20}O_{40}$(0.667) per unit cell. [RuO_6] indicates the six-coordinated Ru atoms in the structure. Ru atoms, green balls; O atoms, red balls.

vectors (1/25 $Å^{-1}$), and the convergence criterion for the atomic force was set to be 0.01 eV/Å. It should be mentioned that all low-energy structures identified from the G-NN calculation have been further verified by using DFT, and the energetics reported in the work, if not explicitly mentioned, are all from DFT calculations.

2.4. DESW Method for the Transition State Search. The transition states (TSs) for CO oxidation are located by the double-ended surface walking method (DESW).[24] The DESW method operates two structural images starting from the initial state (IS) and final state (FS), respectively, to walk toward each other wisely. Repeated bias potential addition and local relaxation are involved in the surface walking with the constrained Broyden dimer (CBD) method to correct the walking direction.[25] Finally, the TS structure will be identified, which was further confirmed by the vibrational frequency analysis and the extrapolation optimization to the correct IS and FS.

3. RESULTS

3.1. RuO_x Bulk. We start our investigation by exploring a range of RuO_x (O% from 20% to 80%) by using the SSW-NN simulation. While RuO_2 is the only known stable oxide form for the Ru element, these simulations have two purposes: first, to validate the accuracy of G-NN potential at different Ru:O compositions; and second, to identify the likely heterojunctions between Ru and RuO_x. From our previous work, the phase separation often occurs when a composition (i.e., Ru:O ratio) is not thermodynamically stable and tends to disproportionate into the neighboring compositions. The phase separated structure thus contains the stable heterojunction atomic structure, and the related information on OR can be gleaned. In our SSW-NN simulation, we explore more than 20 000 minima for each composition by varying the supercell size from 10 to 30 Ru atoms, from which the global minimum (GM) is obtained.

By using the GM and computing their formation energy (ΔE), we can plot the thermodynamic convex hull for RuO_x, as shown in Figure 1a. The ΔE of RuO_x is defined in eq 2 by referencing the Ru metal (hcp) and gas phase O_2 molecule. Our calculated formation energy ΔE for RuO_2 is −291 kJ/mol, being consistent with the experimental ΔH_f −305 to −315 kJ/mol at the standard state.[2]

$$\Delta E = \frac{E_{Ru_xO_y} - xE_{Ru} - \frac{y}{2}E_{O_2}}{y} \quad (2)$$

While the thermodynamics diagram exhibits three convex points for RuO_x, i.e., Ru_2O, RuO, and RuO_2, only RuO_2 (O% = 0.667) has the distinct single phase crystal structure, i.e., the rutile structure with all Ru atoms in the octahedron coordination [RuO_6]. The Ru_2O and RuO are the biphase crystals glued by metal Ru and RuO_2, and Ru_2O_3 is a concave point in the thermodynamics diagram, with Ru metal clusters dissolved in RuO_2 (see Figure 1d). In fact, by analyzing the GM at different Ru:O ratios, we found that the octahedron [RuO_6] unit appears as early as O% = 0.25 (Ru_3O), as depicted in Figure 1b−e, and with the increase of O content, the rutile structure of RuO_2 becomes more popular. Above O% = 0.667, the isolated tetrahedral [RuO_4] units start to form in the vacuum region of the supercell (see Figure S1), which can be considered as the evaporated RuO_4 molecules from RuO_2 in the excess of O supply. Therefore, based on the global structure exploration, we confirm that no thermodynamically stable bulk crystal structures for Ru_2O_3 and RuO_3 are present.

Interestingly, apart from the GM structures, we have identified many different interface structures between RuO_2 and Ru that form into a biphase crystal. Certainly, the most stable one of them is like what appeared in the GM of Ru_2O and RuO in Figure 1b,c, which follows the same orientation relationship (OR), namely, OR_1: $(10\bar{1}0)_{Ru}//(101)_{RuO_2}$; $[0001]_{Ru}//[010]_{RuO_2}$ (also, see Section 3.2). The OR includes a pair of parallel crystallography planes $(hkl)_{P1}//(hkl)_{P2}$ of two

https://doi.org/10.1021/acs.jpcc.1c04858
J. Phys. Chem. C XXXX, XXX, XXX−XXX

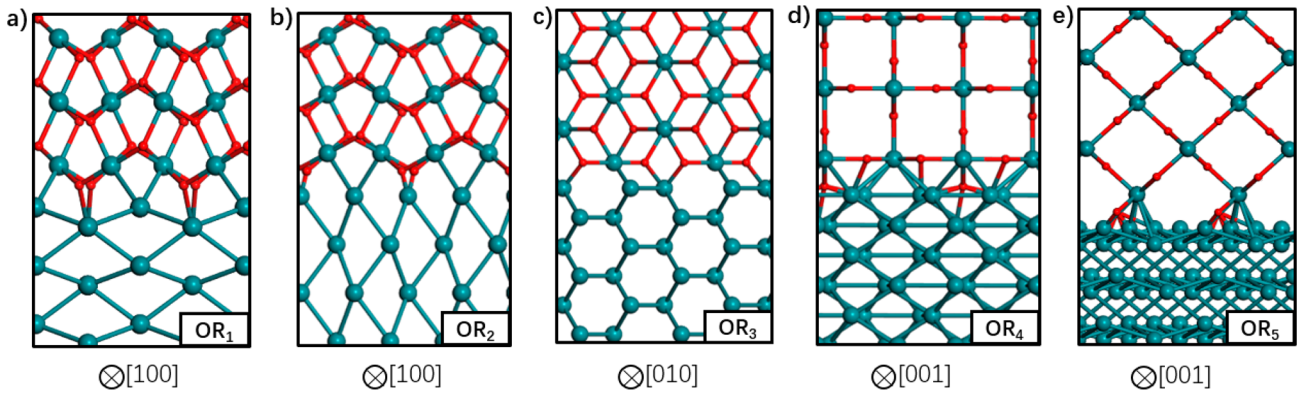

Figure 2. Atomic structures of five Ru−RuO_2 interfaces with different ORs, see also Table 1 for details. Ru atoms, green balls; O atoms, red balls. The crystallographic direction in RuO_2 bulk is indicated.

phases (P1 and P2) that are attached to each other (with lattice parameters *a* and *b*) and a pair of parallel directions $[uvw]_{P1}//[uvw]_{P2}$. These results thus imply that the oxidation of Ru metal could form epitaxial layers of RuO_2 on Ru by forming a structure-matched interface. In the next subsection, we will combine the SSW method and the modified PTMC theory to identify all of the likely interfaces between Ru and RuO_2.

3.2. Heterojunction between Ru and RuO_2. The PTMC theory provides a rigorous way to construct a heterojunction by matching the lattice between two different crystals. However, the atomic positions at the interface cannot be properly optimized by the PTMC method. The modified PTMC method utilized here for the interface structure search combines the PTMC method with SSW global optimization to achieve both the lattice match and interfacial atomic position optimization.

In our search of stable interfaces, the possible ORs with low strain (typically <10%) were first screened out by using the PTMC theory. For each OR, we constructed several initial guess structures by manually joining the two surfaces in one supercell. By further performing SSW global optimization starting from these initial structures, we obtained the GM structure and then evaluated their stability by using eq 3 to compute the interfacial energy (γ_{int}).

$$\gamma_{int} = \frac{E_{Ru_xO_y} - \left(x - \frac{y}{2}\right)E_{Ru} - \frac{y}{2}E_{RuO_2}}{2A} \quad (3)$$

In eq 3, $E_{Ru_xO_y}$ is total energy for the interface Ru_xO_y, and E_{Ru} and E_{RuO_2} are the total energy of bulk metal Ru and RuO_2, respectively. The denominator *A* is the interfacial area in a heterojunction. To compare different interfaces, we always utilize six layers of Ru and three layers of RuO_2 in computing the interfacial energy. We finally identified five lowest-energy Ru−RuO_2 interfaces with the distinct OR, named from OR_1 to OR_5 as listed below, and their structures are shown in Figure 2a. We will elaborate these interfaces in the following paragraphs.

OR_1: $(10\bar{1}0)_{Ru}//(101)_{RuO_2}$; $[0001]_{Ru}//[010]_{RuO_2}$

OR_2: $(0001)_{Ru}//(101)_{RuO_2}$; $[10\bar{1}0]_{Ru}//[010]_{RuO_2}$

OR_3: $(11\bar{2}0)_{Ru}//(001)_{RuO_2}$; $[0001]_{Ru}//[100]_{RuO_2}$

OR_4: $(11\bar{2}0)_{Ru}//(110)_{RuO_2}$; $[01\bar{1}2]_{Ru}//[110]_{RuO_2}$

OR_5: $(10\bar{1}0)_{Ru}//(100)_{RuO_2}$; $[01\bar{1}0]_{Ru}//[102]_{RuO_2}$

The OR_1 interface, $(10\bar{1}0)_{Ru}//(101)_{RuO_2}$, is the most stable interface between Ru and RuO_2 (Figure 2a) and has been seen in the GM of bulk crystals mentioned in Section 3.1. The interfacial energy of this interface is 2.42 J/m^2 with the maximal strain of 4.8% along $[0001]_{Ru}//[010]_{RuO_2}$ (see Table 1). Each interfacial Ru atom bonds with two Ru atoms of the metallic phase and five O atoms of the oxide phase, while each interfacial O atom bonds with two Ru atoms of each phase. As a result, the O coordination number (CN(O)) of the interfacial Ru atoms is five, one less than that in bulk RuO_2, while the Ru coordination number (CN(Ru)) of interfacial O is four, one more than that in bulk RuO_2. The bond distances at the interface are generally close to their counterpart in the bulk. For example, the bond lengths between the interfacial Ru atoms and O atoms of the oxide phase (d_{Ru-O}) are 1.97 and 1.90 Å, while they are 2.01 and 1.97 in RuO_2 bulk. The bond length between the interfacial Ru atoms and Ru atoms of the metallic phase (d_{Ru-Ru}) is 2.54 Å, slightly smaller than that of bulk Ru atoms, 2.66 Å.

Table 1. Structural Parameters of the Five Most Stable Ru−RuO_2 Interfaces

structural parameters		OR_1	OR_2	OR_3	OR_4	OR_5
	γ_{int} (J/m^2)	2.42	2.48	2.72	2.88	3.39
	strain (%)	4.8	3.6	5.3	1.6	9.2
metallic phase	*a* (Å)	4.32	5.47	4.27	6.40	5.01
	b (Å)	5.49	4.72	4.75	6.39	9.21
	γ (deg)	90	90	90	90	86.3
oxide phase	*a* (Å)	4.54	5.52	4.54	6.42	4.54
	b (Å)	5.53	4.55	4.55	6.29	9.43
	γ (deg)	90	90	90	90	90

The OR_2 interface, $(0001)_{Ru}//(101)_{RuO_2}$, involves the close-packed plane of Ru metal, i.e., (0001), at the interface (Figure 2b), and its interfacial energy is 2.48 J/m^2, slightly higher than that of OR_1. The lattice match for OR_2 is in fact smaller than that for OR_1, being maximally 3.6% along the $[10\bar{1}0]_{Ru}//[010]_{RuO_2}$ direction. This indicates that the atomic match of OR_2 is poorer than that of OR_1, which causes the higher interfacial energy. The CN(O) and CN(Ru) of the interfacial

https://doi.org/10.1021/acs.jpcc.1c04858
J. Phys. Chem. C XXXX, XXX, XXX−XXX

Ru and O atoms are five and four, respectively, the same as those in the OR_1 interface. The d_{Ru-O} values are 2.01 and 2.00 Å, which are longer than that in OR_1. The d_{Ru-Ru} is 2.51 Å, slightly shorter than that in OR_1.

The OR_3 interface, $(11\bar{2}0)_{Ru}//(001)_{RuO_2}$, has an interfacial energy of 2.72 J/m^2 with the leading strain of 5.3% along the $[0001]_{Ru}//[100]_{RuO_2}$ direction (Figure 2c). Each interfacial Ru atom bonds with three Ru atoms of the metallic phase and four O atoms of the oxide phase, instead of two and five in OR_1 and OR_2. The d_{Ru-O} values are 2.00 and 1.95 Å, in between those in OR_1 and in OR_2. The d_{Ru-Ru} is 2.58 Å, the longest among OR_1-OR_3.

The OR_4 interface, $(11\bar{2}0)_{Ru}//(110)_{RuO_2}$, has the lowest lattice strain (1.6% along the $[01\bar{1}2]_{Ru}//[110]_{RuO_2}$ direction), but the interfacial energy (2.88 J/m^2) only ranks the fourth among the interfaces. The coordination numbers for the interfacial Ru atoms are the same as those in OR_1, wherein each interfacial O atom coordinates with five Ru atoms, three in Ru metal and two in RuO_2. The d_{Ru-O} values are 2.12 and 1.91 Å, the longest among all interfaces, which is close to those in the $RuO_2(110)$ surface; the d_{Ru-Ru} is 2.44 Å, the smallest among the five interfaces.

The OR_5 interface, $(10\bar{1}0)_{Ru}//(100)_{RuO_2}$ (Figure 2e), has the highest interfacial energy 3.39 J/m^2 with the largest strain of 9.2%. In line with its poorest stability, most Ru atoms of the metal phase are not coordinated with O atoms in the oxide phase, leaving vacuum regions at the interface. The d_{Ru-O} values are 2.01 and 1.97 Å, and the d_{Ru-Ru} is 2.64 Å.

It is interesting to compare our theoretically predicted interfaces with those observed in experiments. We note that while there is no atomic information on the interface between RuO_2 and Ru, RuO_2 has been commonly prepared by oxidizing Ru metal in experiments, e.g. by using chemical vapor transport in a flowing oxygen system.[2] In these experiments, the $RuO_2(101)$ facet was reported to present on most of the growth habits and thus appeared to be the predominant orientation.[2,8] This is consistent with the fact that the two lowest-energy interfaces, OR_1 and OR_2, both contain $RuO_2(101)$ but with different Ru metal facets. In addition, multiple growth modes were also observed in scanning tunneling microscopy (STM) experiments:[6] on the $Ru(10\bar{1}0)$ surface, not only does the (100) orientation of RuO_2 grow, but also, the $RuO_2(101)$ and the $RuO_2(110)$ surfaces (to the lesser extent) grow. The two leading growth modes agree with our OR_1 and OR_5. The appearance of $RuO_2(110)$ might be due to the reconstruction since $RuO_2(110)$ has the lowest surface energy. Our predicted OR_3 and OR_4 have not been explicitly observed or mentioned in the literature.

3.3. RuO_x Thin Layers on Ru. The knowledge on the energetically favored OR provides the structural basis to gradually grow oxide layers on Ru metal and evaluate their stability, particularly for thin films. Considering that $RuO_2(101)$ has been well observed in experiments and forms the most stable interface OR_1, we focused on $RuO_2(101)$ thin layers on $Ru(10\bar{1}0)$ for CO oxidation activity. In growing the $RuO_2(101)$ thin layer, we gradually added O atoms onto the Ru surface and performed SSW-NN global optimization at each O coverage. A series of GM of RuO_x/Ru interface structures were thus obtained, which are utilized to evaluate the thermodynamic stability at different O coverages, up to 6 monolayer (ML) O, by using eq 4. The O coverage is with respect to the surface exposed Ru atom. In computing the chemical potential of O (μ_O), the reaction condition is set as the typical condition in experiments; i.e., the temperature (T) and the O_2 pressure (p) are 700 K and 0.01 mbar, respectively.[10]

$$\Delta G = \frac{E_{Ru_xO_y} - xE_{Ru} - y\mu_O}{y} \quad (4)$$

Figure 3g shows the calculated formation free energy ΔG for thin layers at different O coverages. Compared to the thick

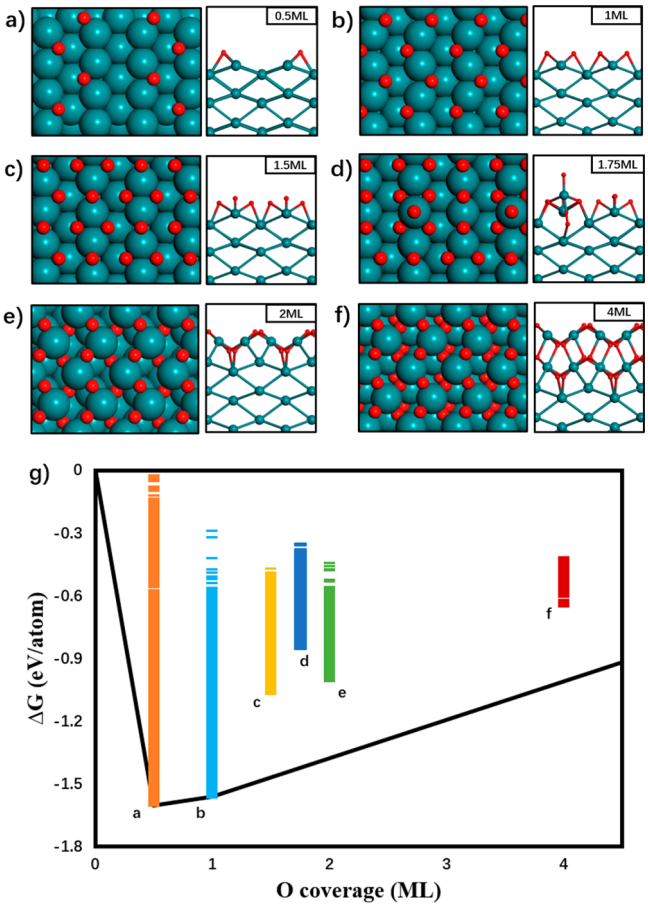

Figure 3. (a−f) Top and side view of $Ru(10\bar{1}0)$ surface structures at the different O coverages from 0.5 to 4 ML. Ru atoms, green balls; O atoms, red balls. (g) Gibbs free energy changes for O adsorption on $Ru(10\bar{1}0)$ at 700 K, $p(O_2)$ = 0.01 mbar with the increase of O coverage.

overlayer with O 6 ML, there are only two convex points, i.e., 0.5 and 1 ML, where the O atoms adsorb on the $Ru(10\bar{1}0)$ surface. At the 0.5 ML, each O is three-coordinated with Ru, forming two bonds with the topmost Ru atoms and one with the second layer Ru. The O atoms form the zigzag chains along the $[1\bar{2}10]$ direction, and separated by one empty trough, the neighboring O zigzag chains shift by one lattice unit along the $[1\bar{2}10]$ direction, forming an overall $c(2 \times 4)$-2O phase. This GM structure at 0.5 ML O has indeed been characterized previously by using LEED experiments and DFT calculations.[26] With the increase of the O coverage to 1 ML, the empty troughs at the 0.5 ML are occupied by the new O zigzag chain along the $[1\bar{2}10]$ direction, and all O zigzag chains have

https://doi.org/10.1021/acs.jpcc.1c04858
J. Phys. Chem. C XXXX, XXX, XXX−XXX

the same periodicity, making a (2 × 1)*p2mg*-2O phase also known in experiments (Figure 3b).[26,27]

The further addition of O atoms onto the surface starts to grow the bridging O, as illustrated by the (1 × 1)-O phase at 1.5 ML (see Figure 3c). At this coverage, every surface Ru atom is coordinated with three O atoms, in comparison with one and two at the 0.5 and 1 ML O coverage, respectively. The bond distance between O_{br} and Ru is generally shorter, 1.94 Å, than that of the adsorbed O atoms at the hollow site (1.98−2.07 Å).

We note that the oxide characteristics emerge only when the O coverage exceeds 1.75 monolayer (ML), as reflected by the formation of Ru cations. Figure 3d shows that about one-fourth of original topmost Ru atoms are pushed significantly out of the surface plane, which reaches the octahedral coordination ([RuO_6]) with six neighboring O atoms, including one terminal O, a geometry similar to Ru cations in RuO_2 bulk. It should be mentioned that the bond length between the terminal O and Ru cation is relatively short, 1.71 Å, smaller than the average Ru−O distance (2.01 Å) in RuO_2 bulk, and the Ru−O distance (1.98 Å) for adsorbed O atoms on the Ru surface.

The GM structures above 2 ML O coverage are found to be the epitaxially grown RuO_2(101) overlayers on Ru(10$\bar{1}$0), as illustrated in Figure 3e,f. These thin RuO_2(101) films are thermodynamically unstable compared to thick layers, apparently because of the lattice mismatch between metal and oxide. For example, the two-layer RuO_2(101), i.e., Figure 3f, the 4 ML O coverage, is −0.65 eV per O atom more stable than the one-layer RuO_2(101) but less stable than the three-layer oxide overlayer. The two-layer RuO_2(101) exhibits Ru_{cus} sites and O_{br} sites with the Ru−O bond length (2.00 and 1.98 Å), already close to their counterparts in the bulk truncated RuO_2(101) (2.01 and 1.97 Å). This implies that the bonding properties of the thin oxide film converge quickly to those of the RuO_2(101) surface, although they are still less stable than thick layers.

3.4. Reaction. Next, we investigated CO oxidation on the O overlayer structures, from O/Ru to RuO_x/Ru. In addition to the CO oxidation on the clean Ru(10$\bar{1}$0) and the RuO_2(110), RuO_2(101) has also been computed for a comparison. In general, there are multiple pathways for CO reacting with O on these surfaces due to multiple O species on the surface. In our studies, we particularly distinguished the terminal O (O_t, one coordination with Ru) from the bridging (O_{br}) or the hollow site (O_{hol}) O atoms, since their reactivity was known to be vastly different for CO oxidation on RuO_2(110). The initial configuration for CO is always considered to be at the most stable adsorption site. Two lowest-energy pathways, if available, for CO reacting with O_t and reacting with O_{br} or O_{hol}, respectively, have been searched for all the surfaces, and these results are listed in Table 2. Also listed in Table 2 are the O atom and CO adsorption energy on these surfaces.

For CO oxidation on the corrugated metal surface Ru(10$\bar{1}$0), not surprisingly, the reaction has a very high reaction barrier, 1.34 eV. This is largely due to the strong adsorption of both CO and O on the metal surface (see Table 2). For CO oxidation on two oxide surfaces, RuO_2(101) and RuO_2(110), the activity on RuO_2(110) is better than that on RuO_2(101), but both of them are much more active than Ru metal. The reaction barrier for CO reacting with the O_t is always lower, 0.77 eV on RuO_2(110) and 0.84 eV on RuO_2(101), while that for CO reacting with the O_{br} is much more difficult, 0.93 and 1.03 eV on (110) and (101) surfaces, respectively. The activity difference between these two oxide surfaces may be attributed to the stronger O adsorption on the corrugated RuO_2(101) than that on RuO_2(110), as indicated in Table 2.

Table 2. CO Oxidation on Ru(10$\bar{1}$0), RuO_2 Surfaces, and Surface Oxides of Ru(10$\bar{1}$0) (RuO_x/Ru)[a]

surface		E_{ad}(O)[b] (t/b/h)	E_{ad}(CO)	E_a
Ru(10$\bar{1}$0)		−2.73(h)	−1.94	1.34
RuO_2(101)		−0.92(t)	−1.39	0.84
		−2.97(b)	−1.39	1.03
RuO_2(110)		−0.81(t)	−1.41	0.77; (0.70−0.92)[c]; (0.89)[d]
		−2.42(b)	−1.41	0.93; (0.74−1.30);[c] (0.86)[d]
RuO_x/Ru(10$\bar{1}$0)	0.5[e]	−2.71(h)	−1.80	1.59
	1	−2.57(h)	−0.42	1.64
	1.75	−1.79(t)	−0.37	0.66
	1.75	−1.34(b)	−0.37	2.70
	4	−0.76(t)	−1.37	0.63
	4	−2.07(b)	−1.37	0.90

[a]All energy units are in eV. [b]t/b/h in parentheses indicates the terminal, bridging, or hollow site adsorption. [c]E_a from previous DFT calculations (refs 28−33). [d]E_a from experiments (ref 34). [e]O coverage in ML on Ru(10$\bar{1}$0).

We have compared our calculated CO oxidation barriers on RuO_2(110) with the data reported in the literature. The barrier of CO + O_t is 0.70−0.92 eV, while that of CO + O_{br} varies significantly, ranging from 0.74 to 1.30 eV.[28−33] The barrier measured in experiment is 0.89 and 0.86 eV for CO reacting with O_t and O_{br}, respectively. We note that Kiejna et al.[33] have compared systematically the DFT results with different pseudopotentials[29,31] and with full potentials.[32] The barriers of CO + O_t and O_{br} are 0.81 and 1.03 eV with full potentials, respectively. Our calculated barriers, 0.77 and 0.93 eV, are consistent with these data.

Now, we turn to CO oxidation on the RuO_x/Ru interface structures. The CO activity follows the rule identified above; i.e., the activity increases sharply once the oxide appears. As shown in Table 2, on the *c*(2 × 4)-2O phase (0.5 ML O), CO is reluctant to recombine with the O atoms adsorbed at the hollow sites (O_{hol}), where the calculated barrier is 1.59 eV. Similarly, when the O coverage reaches 1 ML, the (2 × 1) *p2mg*-2O phase, the barrier of CO + O_{hol} remains high, 1.64 eV. In both cases, the O atoms adsorb at the hcp hollow site of the metal surface (we have attempted to optimize the O atom at the top site on Ru(10$\bar{1}$0), which however leads to O relaxation to the neighboring hollow site).

In contrast, for CO oxidation on the 1.75 ML O adsorbed Ru(10$\bar{1}$0), the barrier for CO reacting with the terminal O reduces suddenly to 0.66 eV, apparently because of the formation of cationic Ru. CO cannot, however, react with the bridging O (E_a = 2.70 eV). Ongoing to the O coverage 4 ML, the two layers of RuO_2(101), CO can now react with both the O_t and the O_{br}, and the calculated barriers are 0.63 and 0.90 eV, respectively.

It is of interest to compare CO oxidation on the thin film RuO_2 with that on RuO_2(101). The initial state (IS) and the transition state (TS) for CO reacting with the terminal O on two surfaces are highlighted in Figure 4. On both surfaces, CO

https://doi.org/10.1021/acs.jpcc.1c04858
J. Phys. Chem. C XXXX, XXX, XXX−XXX

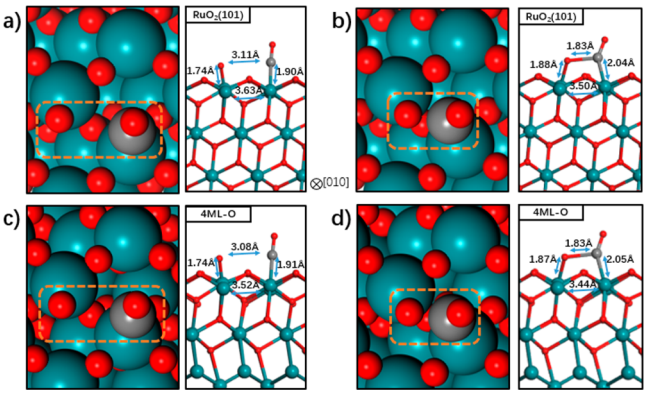

Figure 4. CO + O_t on $RuO_2(101)$ [(a) initial state; (b) transition state] and on Ru(10$\bar{1}$0) with 4 ML O coverage [(c) initial state, (d) transition state]. Ru atoms, green balls; O atoms, red balls; C atoms, gray balls.

adsorbs on the top site of a Ru_{cus}, and the terminal O is on the top site of a nearby Ru_{cus}. Due to the lattice compression of the RuO_2 grown on Ru, the distance between the two Ru_{cus} atoms where CO and O_t adsorb decreases to 3.52 Å (cf. 3.63 Å in $RuO_2(101)$). Consistently, the initial CO and O_t separation on the thin film is slightly smaller, 3.08 Å, while that on $RuO_2(101)$ is 3.11 Å. The C−Ru distances and O−Ru distances on the thin film are quite close to those on $RuO_2(101)$, and the structures at the TSs are also identical, with the OC−O distance being 1.83 Å in both cases. However, the adsorption energies for the O atoms and CO at the IS on the thin film are obviously lower (see Table 2), suggesting the weaker bonding due to the compressed lattice of the oxide layer. The barriers of CO oxidation on the thin film are consistently lower than that on the oxide surface, 0.63 vs 0.84 eV for CO + O_t and 0.90 vs 1.03 eV for CO + O_{br}. The activity increase should thus be caused by the weakened CO and O bonding on the strained thin film.

4. DISCUSSION

Our results demonstrate quantitatively that the RuO_2 thin film on Ru metal is not thermodynamically stable. This implies that the oxidation of Ru metal cannot be self-inhibited kinetically by forming the dense oxide coating, which is different from metals such as Al where the passive oxide film can form. The fundamental reason for this phenomenon can be attributed to the large lattice mismatch, i.e., 4.8%, for the most stable interface $(10\bar{1}0)_{Ru}//(101)_{RuO_2}$. The nucleation and growth mode of RuO_x on Ru can thus be classified as an autocatalytic oxidation process,[35] consistent with the in situ surface X-ray diffraction (SXRD) measurements.[36] In addition, the oxide grown on the dominant metal surface, i.e., the close-packed (0001) surface, is even less stable: for the interface $(0001)_{Ru}//(101)_{RuO_2}$, although the lattice mismatch becomes smaller (3.6%), the interface energy increases due to the atomic mismatch (poor coordination) at the interface. We also confirm that the adsorbed O overlayer on the Ru metal can be thermodynamically stable with the maximum coverage up to 1 ML on (10$\bar{1}$0), which was observed by surface science experiments.[26,27]

In line with the simple RuO_x bulk chemistry where only RuO_2 is thermodynamically stable, we notice that there is essentially no transition phase from the adsorbed O overlayer to the oxide film. The oxide feature as indicated by the [RuO_6] coordination appears at the 1.75 ML O coverage, and a single layer of RuO_2 thin film emerges immediately at the 2 ML O coverage. The high tendency to form the RuO_2 crystal structure on the surface must come from the strong preference of RuO_2 rutile phase as indicated by the bulk thermodynamics diagram.

To better understand the structure evolution, we have plotted the projected d band for the Ru atoms on the Ru(10$\bar{1}$0) surface at different O coverages in Figure 5. As

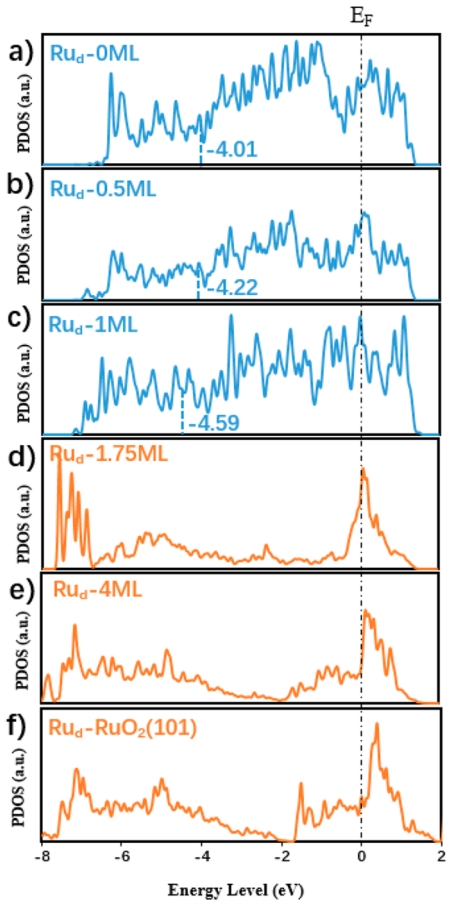

Figure 5. Projected DOS of Ru 4d states on six surfaces: Ru(10$\bar{1}$0) with the coverage of O = 0 ML (a), 0.5 ML (b), 1 ML (c), 1.75 M L(d), 4 ML (e), and $RuO_2(101)$ surface (f). E_F indicates the Fermi level. The position of the d band center is denoted by the blue dashed line.

shown, the d band of Ru does not change significantly for O coverages below 1 ML, where Ru atoms belong to metal. The d band spreads widely from −7 to +1.2 eV with a significant density of states at the Fermi level, which reflects the metallic bonding. The presence of the surface O atoms downshifts the band center from −4.01 eV of the clean metal surface to −4.22 eV at 0.5 ML O and to −4.59 eV at 1 ML O but hardly affects the overall shape of the d band. In contrast, at the 1.75 ML, the d band of the Ru atom in [RuO_6] splits clearly into two major peaks, one at ∼−7.5 eV and the other around the Fermi level. The major peak around the Fermi level is mainly contributed from the terminal O associated with cationic Ru. These low-energy empty states can thus take part in CO oxidation by accepting the 5σ electron, yielding the high activity of terminal O. The d band splitting is a consequence of the Ru−O

https://doi.org/10.1021/acs.jpcc.1c04858
J. Phys. Chem. C XXXX, XXX, XXX−XXX

covalent bonding, suggesting that the cationic Ru develops strong covalent bonding with the O ligand. With the further increase of O coverage, the Ru d band of the oxide film remains largely the same as that of [RuO_6] at the 1.75 ML, except that the bonding and the antibonding peaks become broader. At the O coverage 4 ML, the Ru d band is very close to that in the RuO_2 surface, which explains their similar activity toward CO oxidation.

5. CONCLUSIONS

By developing the first Ru−C−H−O G-NN potential, this work explores systematically RuO_x structures from bulk to interfaces and compares their CO oxidation activity. The good accuracy and fast computation speed of G-NN potential not only benefit the search of structure phase space in bulk and on surfaces but also allow the combination with the phenomenological theory of martensitic crystallography to quickly evaluate the interface stability. Our main results are outlined as follows:

(i) The Ru−C−H−O quaternary G-NN potential is established by learning the 46 731 DFT data set from SSW global exploration. The root-mean-square (rms) errors of the G-NN potential are 7.684 meV/atom and 0.200 eV/Å for the energy and the force.

(ii) The RuO_x bulk thermodynamics phase diagram is determined, which shows that RuO_2 is the only thermodynamically stable phase at the ambient conditions. There is no stable crystal phase for Ru_2O_3 and RuO_3.

(iii) Among five relatively stable interfaces obtained from the modified PTMC interface search, the two most stable interfaces are all related to the corrugated RuO_2(101) plane, which can epitaxially grow on both Ru(10$\bar{1}$0) and (0001). The most stable RuO_2(110) plane is not the preferential plane to grow on Ru metal.

(iv) On Ru(10$\bar{1}$0), the oxide starts to form above 1.75 ML O coverage. A RuO_2(101) thin layer appears immediately after 2 ML O coverage. The thin RuO_2(101) layers are however thermodynamically stable. This implies that RuO_2 will aggregate into large islands, and the oxidation process will not be stopped until all metal is consumed.

(v) CO oxidation on the metastable RuO_2(101) thin film has the lowest barrier, 0.63 eV for CO reacting with the terminal O and 0.90 eV reacting with the bridging O. These values are lower than those on both RuO_2(110) and RuO_2(101) surfaces. The theoretical results imply the significance to synthesize and optimize metal/oxide phase boundaries, probably via doping and nanostructuring, which may lead to the superior catalytic activity caused by the lattice and atomic mismatch.

■ ASSOCIATED CONTENT

Supporting Information

The Supporting Information is available free of charge at https://pubs.acs.org/doi/10.1021/acs.jpcc.1c04858.

Theoretical methodology and construction of the quaternary Ru−C−H−O G-NN potential; modified phenomenological theory of martensitic crystallography; structures for the GM of RuO_x; XYZ coordinates for important structures of RuO_x bulk, the interfaces between Ru and RuO_2 RuO_x/Ru(10$\bar{1}$0); and the IS and TS for CO oxidation (PDF)

■ AUTHOR INFORMATION

Corresponding Authors

Ye-Fei Li − *Collaborative Innovation Center of Chemistry for Energy Material, Shanghai Key Laboratory of Molecular Catalysis and Innovative Materials, Key Laboratory of Computational Physical Science, Department of Chemistry, Fudan University, Shanghai 200433, China;* orcid.org/0000-0003-4433-7433; Email: yefeil@fudan.edu.cn

Zhi-Pan Liu − *Collaborative Innovation Center of Chemistry for Energy Material, Shanghai Key Laboratory of Molecular Catalysis and Innovative Materials, Key Laboratory of Computational Physical Science, Department of Chemistry, Fudan University, Shanghai 200433, China;* orcid.org/0000-0002-2906-5217; Email: zpliu@fudan.edu.cn

Authors

Ze-Yi Zhu − *Collaborative Innovation Center of Chemistry for Energy Material, Shanghai Key Laboratory of Molecular Catalysis and Innovative Materials, Key Laboratory of Computational Physical Science, Department of Chemistry, Fudan University, Shanghai 200433, China*

Cheng Shang − *Collaborative Innovation Center of Chemistry for Energy Material, Shanghai Key Laboratory of Molecular Catalysis and Innovative Materials, Key Laboratory of Computational Physical Science, Department of Chemistry, Fudan University, Shanghai 200433, China;* orcid.org/0000-0001-7486-1514

Complete contact information is available at: https://pubs.acs.org/10.1021/acs.jpcc.1c04858

Notes

The authors declare no competing financial interest.

■ ACKNOWLEDGMENTS

This work was supported by the National Key Research and Development Program of China (2018YFA0208600) and the National Science Foundation of China (22033003, 21533001, and 91745201).

■ REFERENCES

(1) Over, H.; Kim, Y. D.; Seitsonen, A. P.; Wendt, S.; Lundgren, E.; Schmid, M.; Varga, P.; Morgante, A.; Ertl, G. Atomic-scale Structure and Catalytic Reactivity of RuO_2. *Science* **2000**, *287*, 1474−1476.

(2) Over, H. Surface Chemistry of Ruthenium Dioxide in Heterogeneous Catalysis and Electrocatalysis: From Fundamental to Applied Research. *Chem. Rev.* **2012**, *112*, 3356−3426.

(3) Gao, F.; Goodman, D. W. CO Oxidation over Ruthenium: Identification of the Catalytically Active Phases at Near-atmospheric Pressures. *Phys. Chem. Chem. Phys.* **2012**, *14*, 6688−6697.

(4) Lin, W. F.; Zei, M. S.; Kim, Y. D.; Over, H.; Ertl, G. Electrochemical versus Gas-Phase Oxidation of Ru Single-Crystal Surfaces. *J. Phys. Chem. B* **2000**, *104*, 6040−6048.

(5) Kim, Y. D.; Schwegmann, S.; Seitsonen, A. P.; Over, H. Epitaxial Growth of RuO_2(100) on Ru(10$\bar{1}$0): Surface Structure and Other Properties. *J. Phys. Chem. B* **2001**, *105*, 2205−2211.

(6) Over, H.; Seitsonen, A. P.; Knapp, M.; Lundgren, E.; Schmid, M.; Varga, P. Visualization of Atomic Processes on Ruthenium Dioxideusing Scanning Tunneling Microscopy. *ChemPhysChem* **2004**, *5*, 167−174.

(7) Zhang, H. J.; Lu, B.; Lu, Y. H.; Xu, Y. F.; Li, H. Y.; Bao, S. N.; He, P. Growth of RuO_2 Thin Layer on Ru(10$\bar{1}$0) Studied by Scanning Tunneling Microscopy. *Surf. Sci.* **2007**, *601*, 2297−2301.

(8) Kim, Y. D.; Over, H.; Krabbes, G.; Ertl, G. Identification of RuO_2 as the Active Phase in CO Oxidation on Oxygen-rich Ruthenium Surfaces. *Top. Catal.* **2000**, *14*, 95−100.

(9) Kim, Y. D.; Seitsonen, A. P.; Wendt, S.; Wang, J.; Fan, C.; Jacobi, K.; Over, H.; Ertl, G. Characterization of Various Oxygen Species on an Oxide Surface: RuO_2(110). *J. Phys. Chem. B* **2001**, *105*, 3752−3758.
(10) Knapp, M.; Seitsonen, A. P.; Kim, Y. D.; Over, H. Catalytic Activity of the RuO2(100) Surface in the Oxidation of CO. *J. Phys. Chem. B* **2004**, *108*, 14392−14397.
(11) Huang, S. D.; Shang, C.; Zhang, X. J.; Liu, Z. P. Material Discovery by Combining Stochastic Surface Walking Global Optimization with a Neural Network. *Chem. Sci.* **2017**, *8*, 6327−6337.
(12) Huang, S. D.; Shang, C.; Kang, P. L.; Liu, Z. P. Atomic Structure of Boron Resolved Using Machine Learning and Global Sampling. *Chem. Sci.* **2018**, *9*, 8644−8655.
(13) Shang, C.; Liu, Z. P. Stochastic Surface Walking Method for Structure Prediction and Pathway Searching. *J. Chem. Theory Comput.* **2013**, *9*, 1838−1845.
(14) Shang, C.; Zhang, X. J.; Liu, Z. P. Stochastic Surface Walking Method for Crystal Structure and Phase Transition Pathway Prediction. *Phys. Chem. Chem. Phys.* **2014**, *16*, 17845−17856.
(15) Huang, S. D.; Shang, C.; Kang, P. L.; Zhang, X. J.; Liu, Z. P. LASP: Fast global potential energy surface exploration. *Wiley Interdiscip. Rev.: Comput. Mol. Sci.* **2019**, *9*, e1415.
(16) Kang, P. L.; Shang, C.; Liu, Z. P. Glucose to 5-Hydroxymethylfurfural: Origin of Site-Selectivity Resolved by Machine Learning Based Reaction Sampling. *J. Am. Chem. Soc.* **2019**, *141*, 20525−20536.
(17) Bain, E. C.; Dunkirk, N. Y. The nature of martensite. *Trans. AIME* **1924**, *70*, 25−46.
(18) Li, Y. F. First Principles Simulations for Morphology and Structural Evolutions of Catalysts in Oxygen Evolution Reaction. *ChemSusChem* **2019**, *12*, 1846−1857.
(19) Li, L. F.; Li, Y. F.; Liu, Z. P. CO_2 Photoreduction via Quantum Tunneling: Thin-TiO_2-Coated GaP with Coherent Interface to Achieve Electron Tunneling. *ACS Catal.* **2019**, *9*, 5668−5678.
(20) Li, Y. F.; Liu, Z. P. Structure Prediction of Heterojunction Interfaces and the Application of AutoInterface Program. *Chem. J. Chinese Universities.* **2020**, *41* (11), 2383−2392.
(21) Kresse, G.; Furthmüller, J. Efficient Iterative Schemes for Ab Initio Total-Energy Calculations Using a Plane-Wave Basis Set. *Phys. Rev. B: Condens. Matter Mater. Phys.* **1996**, *54*, 11169−11186.
(22) Kresse, G.; Joubert, D. From Ultrasoft Pseudopotentials to the Projector Augmented-Wave Method. *Phys. Rev. B: Condens. Matter Mater. Phys.* **1999**, *59*, 1758−1775.
(23) Perdew, J. P.; Burke, K.; Ernzerhof, M. Generalized Gradient Approximation Made Simple. *Phys. Rev. Lett.* **1996**, *77*, 3865−3868.
(24) Zhang, X.-J.; Shang, C.; Liu, Z.-P. Double-Ended Surface Walking Method for Pathway Building and Transition State Location of Complex Reactions. *J. Chem. Theory Comput.* **2013**, *9*, 5745−5753.
(25) Shang, C.; Liu, Z.-P. Constrained Broyden Dimer Method with Bias Potential for Exploring Potential Energy Surface of Multistep Reaction Process. *J. Chem. Theory Comput.* **2012**, *8*, 2215−2222.
(26) Schwegmann, S.; Seitsonen, A. P.; De Renzi, V.; Dietrich, H.; Bludau, H.; Gierer, M.; Over, H.; Jacobi, K.; Scheffler, M.; Ertl, G. Oxygen Adsorption on the Ru(10$\bar{1}$0) Surface: Anomalous Coverage Dependence. *Phys. Rev. B: Condens. Matter Mater. Phys.* **1998**, *57*, 15487−15495.
(27) Zhang, H. J.; Lu, B.; Li, H. Y.; Bao, S. N.; He, P. Scanning Tunneling Microscopy and Ultraviolet Photoemission Spectroscopy Studies of Oxygen Adsorption on Ru(10$\bar{1}$0). *Surf. Sci.* **2004**, *556*, 63−68.
(28) Seitsonen, A. P.; Kim, Y. D.; Knapp, M.; Wendt, S.; Over, H. CO Adsorption on the Reduced RuO_2(110) Surface: Energetics and Structure. *Phys. Rev. B: Condens. Matter Mater. Phys.* **2001**, *65*, No. 035413.
(29) Wendt, S.; Seitsonen, A. P.; Over, H. Catalytic activity of RuO_2(110) in the oxidation of CO. *Catal. Today* **2003**, *85*, 167−175.
(30) Seitsonen, A. P.; Over, H. Intimate Interplay of Theory and Experiments in Model Catalysis. *Surf. Sci.* **2009**, *603*, 1717−1723.
(31) Liu, Z. P.; Hu, P.; Alavi, A. Mechanism for the High Reactivity of CO Oxidation on a Ruthenium−oxide. *J. Chem. Phys.* **2001**, *114*, 5956−5957.
(32) Reuter, K.; Scheffler, M. Composition and Structure of the RuO_2(110) Surface in an O_2 and CO Environment: Implications for the Catalytic Formation of CO_2. *Phys. Rev. B: Condens. Matter Mater. Phys.* **2003**, *68*, No. 045407.
(33) Kiejna, A.; Kresse, G.; Rogal, J.; De Sarkar, A.; Reuter, K.; Scheffler, M. Comparison of the Full-potential and Frozen-core Approximation Approaches to Density-functional Calculations of Surfaces. *Phys. Rev. B: Condens. Matter Mater. Phys.* **2006**, *73*, No. 035404.
(34) Farkas, A.; Hess, F.; Over, H. Experiment-Based Kinetic Monte Carlo Simulations: CO Oxidation over RuO_2(110). *J. Phys. Chem. C* **2012**, *116*, 581−591.
(35) Over, H.; Seitsonen, A. P. Oxidation of Metal surface. *Science* **2002**, *297*, 2003−2005.
(36) He, Y. B.; Knapp, M.; Lundgren, E.; Over, H. Ru(0001) Model Catalyst under Oxidizing and Reducing Reaction Conditions: In-Situ High-Pressure Surface X-ray Diffraction Study. *J. Phys. Chem. B* **2005**, *109*, 21825−21830.

https://doi.org/10.1021/acs.jpcc.1c04858
J. Phys. Chem. C XXXX, XXX, XXX−XXX